



● Original Contribution

---

## MEMBRANE PERFORATION AND RECOVERY DYNAMICS IN MICROBUBBLE-MEDIATED SONOPORATION

YAXIN HU,\* JENNIFER M. F. WAN,<sup>†</sup> and ALFRED C. H. YU\*

\*Medical Engineering Program, University of Hong Kong, Pokfulam, Hong Kong; and <sup>†</sup>School of Biological Sciences, University of Hong Kong, Pokfulam, Hong Kong

(Received 25 March 2013; revised 10 June 2013; in final form 4 August 2013)

**Abstract**—Transient sonoporation can essentially be epitomized by two fundamental processes: acoustically induced membrane perforation and its subsequent resealing. To provide insight into these processes, this article presents a new series of direct evidence on the membrane-level dynamics during and after an episode of sonoporation. Our direct observations were obtained from anchored fetal fibroblasts whose membrane topography was imaged *in situ* using real-time confocal microscopy. To facilitate controlled sonoporation at the single-cell level, microbubbles that can passively adhere to the cell membrane were first introduced at a 1:1 cell-to-bubble ratio. Single-pulse ultrasound exposure (1-MHz frequency, 10-cycle pulse duration, 0.85-MPa peak negative pressure *in situ*) was then applied to trigger microbubble pulsation/collapse, which, in turn, instigated membrane perforation. With this protocol, five membrane-level phenomena were observed: (i) localized perforation of the cell membrane was synchronized with the instant of ultrasound pulsing; (ii) perforation sites with temporal peak area  $<30 \mu\text{m}^2$  were resealed successfully; (iii) during recovery, a thickened pore rim emerged, and its temporal progression corresponded with the pore closure action; (iv) membrane resealing, if successful, would generally be completed within 1 min of the onset of sonoporation, and the resealing time constant was estimated to be below 20 s; (v) membrane resealing would fail for overly large pores ( $>100 \mu\text{m}^2$ ) or in the absence of extracellular calcium ions. These findings serve to underscore the spatiotemporal complexity of membrane-level dynamics in sonoporation. (E-mail: alfred.yu@hku.hk) © 2013 World Federation for Ultrasound in Medicine & Biology.

**Key Words:** Sonoporation, Membrane perforation, Membrane recovery, Spatiotemporal dynamics, Real-time confocal imaging, Surface topography.

### INTRODUCTION

The combined use of ultrasound and microbubbles to transiently perforate the cellular membrane has undoubtedly spurred new application opportunities in biomedicine. As highlighted in numerous reviews (Geers et al. 2012; Liang et al. 2010; Nomikou and McHale 2010; Pua and Zhong 2009), this way of achieving membrane perforation (often referred to as *sonoporation*) holds strong potential in enhancing the delivery of large drug molecules and gene plasmids into a cell to induce therapeutic effects. Compared with other membrane perforation approaches, sonoporation is perhaps unique in that spatiotemporal control can be readily exercised. In particular, spatial localization of sonoporation may be realized by introducing synthetic microbubbles as

sonoporation agents in the vicinity of cells (Hernot and Klibanov 2008; Liu et al. 2006; Suzuki et al. 2011). As well, temporal specificity may be achieved in sonoporation by commanding the time of ultrasound application to controllably instigate microbubble pulsation or collapse (corresponding to stable or inertial cavitation, respectively) that generates the mechanical force required for membrane puncturing (Ferrara et al. 2007).

To complement the strong efforts to develop sonoporation-based therapeutic applications, it is vital to establish the details of fundamental biophysical processes involved in sonoporation. Of significant relevance are two membrane-level processes that epitomize the notion of sonoporation: (i) how membrane perforation is induced by ultrasound-microbubble interactions, and (ii) how the membrane remodels itself after an episode of sonoporation. Acquiring direct observation of these processes is, however, not a straightforward task. Although high-resolution images of sonoporated cells

Address correspondence to: Alfred C. H. Yu, Medical Engineering Program, University of Hong Kong, Pokfulam, Hong Kong. E-mail: [alfred.yu@hku.hk](mailto:alfred.yu@hku.hk)

can be obtained using advanced techniques such as atomic force microscopy (Duvshani-Eshet et al. 2006; Prentice et al. 2005; Ross et al. 2002; Zhao et al. 2008) and electron microscopy (Mehier-Humbert et al. 2005; Schlicher et al. 2006, 2010; Qiu et al. 2010; Yang et al. 2008), these approaches are not suitable for examining the temporal dynamics of sonoporation. Also, even though voltage clamping may be used to examine transmembranous ion kinetics related to sonoporation at fine temporal resolution (Deng et al. 2004; Pan et al. 2005; Tran et al. 2008; Zhou et al. 2008), this technique inherently cannot provide image-level information. Alternatively, ultrafast optical microscopy has frequently been leveraged to monitor the spatiotemporal dynamics of microbubble-cell interactions over the course of acoustic cavitation (Kudo et al. 2009; Ohl et al. 2006; Nejad et al. 2011; Sankin et al. 2010; Zhou et al. 2012). However, to examine the details of membrane dynamics (especially during post-sonoporation recovery), optical image contrast seems to be mediocre if not inadequate.

In the investigation described here, we sought to acquire the first series of direct observations on the time-course dynamics of perforation sites in microbubble-mediated sonoporation. Our overall postulate was that, to gain detailed insight into how perforation and recovery take place in sonoporation, it is essential to unravel the time-varying surface topography of sonoporated cell membrane *in situ*. In approaching this task, we surmised that real-time confocal fluorescence microscopy, if coupled to a well-characterized acoustic exposure apparatus, is a suitable experimental methodology because it offers both high imaging contrast (*via* specific labeling of cell membrane) and sufficient temporal resolution (needed to render membrane dynamics over the course of sonoporation). Note that real-time fluorescence imaging was previously introduced in other sonoporation studies to examine subcellular events such as calcium ion influxes (Fan et al. 2010; Juffermans et al. 2009; Kumon et al. 2009; Park et al. 2010) and trans-membranous diffusion of fluorescent markers (Fan et al. 2012; Kooiman et al. 2011; Meijering et al. 2009; van Ruijssevelt et al. 2013). Fixed-cell confocal microscopy of sonoporated cell morphology has also been reported (Schlicher et al. 2006, 2010). In contrast, here our aim was to leverage real-time confocal microscopy to elucidate the time course of membrane perforation and recovery in sonoporation. This sequence of membrane-level events has yet to be convincingly observed *in situ*.

## METHODS

### *Experimental hardware design*

**Ultrasound apparatus and imaging system.** The real-time cell membrane imaging platform used in this

work was a composite apparatus that coupled an ultrasound transmission module to a laser scanning confocal microscopy system (LSM 710, Carl Zeiss, Jena, Germany). As illustrated in Figure 1a, the single-element piston transducer (1-MHz frequency, 25.4-mm diameter; Wuxi Beisheng Technology, Wuxi, Jiangsu, China) of the ultrasound module was driven by a two-stage electronics setup that was an arbitrary waveform generator for pulse shape programming (33120A, Agilent Technologies, Santa Clara, CA, USA) and a 50-dB broadband amplifier (2100L, Electronics & Innovation, Rochester, NY, USA). The nose cone-shaped acrylic waveguide, on which the ultrasound transducer was mounted, was a custom-designed device with 75 mm height and 8 mm nose diameter.

**Cell chamber.** The cell chamber used for experimentation was an in-house design, and a top view of it is shown in the lower left inset of Figure 1a. Modified from a 50 mm-diameter polystyrene dish with 1-mm-thick base (150288, Nunc, Roskilde, Denmark), this chamber housed a 20 × 28-mm<sup>2</sup> observation window within which cells were seeded. The window was created by carving out that particular segment of the polystyrene dish and sealing the base of the resulting void with a cover glass less than 160 µm thick (Type 1, Vitromed, Basel, Switzerland). Note that for 1-MHz ultrasound, the wavelength of which was approximately 1.5 mm in water-solvent solutions, the cover glass can be assumed to be an acoustically thin layer.

**Platform alignment.** A 4-mm detachable tip was included at the nose of the waveguide to facilitate physical alignment between the waveguide, the microscope's scan plane and the cell chamber. The alignment was realized by placing the tip in contact with the base of the cell chamber's observation window and positioning it at the center of the microscope's field of view. This process was visually guided by observing through the microscope's eyepiece. To avoid interfering with the microscope's bright-field imaging operations, the waveguide was angled at 40° with respect to the surface normal of the cell chamber. After the alignment was completed, the 4-mm tip was detached from the nose of the waveguide.

### *Cell preparation protocol*

**Cell culturing.** MRC-5 fetal fibroblasts (CCL-171, American Type Culture Collection, Manassas, VA, USA) were used as our cell model. It is a commonly used cell line in transdermal drug delivery. The cells were first cultured in monolayer form inside a culture flask using minimum essential medium (MEM) (Gibco 41500-018, Invitrogen, Carlsbad, CA, USA) that was supplemented with 10% fetal bovine serum (SV30160.03, Thermo Scientific, Waltham, MA, USA) and 1 mM sodium pyruvate

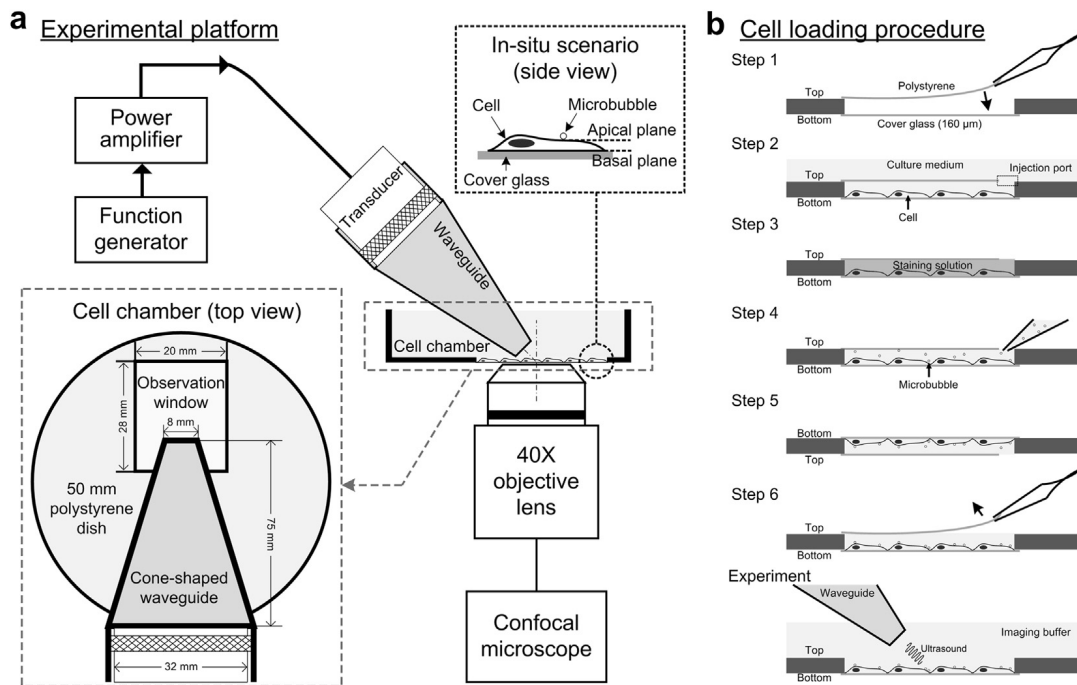


Fig. 1. Experimental methods used for real-time imaging of membrane-level processes in sonoporation. (a) Schematic of the hardware components involved in the experimental platform. Lower-left inset: Top view of the cell chamber. Note that the nose of the waveguide is aligned with the center of the observation window (dimensions are also indicated). Upper inset: Close-up view of the *in situ* orientation of cells, microbubbles and the confocal scan planes (apical and basal).

(b) Procedure for loading cells and microbubbles into the observation window of the cell chamber.

(Gibco 11840-030, Invitrogen). Throughout the culturing, the cells were placed inside a 37°C incubator environment with 5% carbon dioxide. Before the experiment, the fibroblasts were harvested by trypsinizing the cells. The working density of the harvested cell extract was 150,000 cells/mL, as determined with a hemocytometer.

**Cell seeding within cell chamber.** The harvested fibroblasts were seeded onto the cover glass of the cell chamber as follows. First, as illustrated in Figure 1b (Step 1), a polystyrene coverslip was patched onto the upper side of the cell chamber's observation window to create a temporary enclosure. The coverslip was secure-sealed on three sides of the window, and a 1-mm gap was left open on the remaining side to serve as an injection port for substance transfer. After that, 0.6 mL of the trypsinized fibroblast extract (*i.e.*, around 90,000 cells) was pipetted into the enclosure. Their attachment to the bottom cover glass was fostered by adding 5 mL of fresh MEM to the cell chamber and placing it inside the incubator for 24 h (Fig. 1b, Step 2).

**Membrane labeling.** After cell attachment to the cover glass, the cell chamber's MEM was replaced with a staining solution to fluorescently label the cell membrane (Fig. 1b, Step 3). In this work, CellMask Orange (C10045, Invitrogen; absorption maximum: 554 nm, emission maximum: 567 nm) was used to stain membrane phospho-

lipids at a working concentration of 2.5  $\mu$ g/mL. The dye was dissolved in a modified Hanks' balanced salt solution (HBSS) buffer (pH 7.4) containing 137 mM sodium chloride (NaCl), 5.4 mM potassium chloride (KCl), 0.25 mM sodium phosphate, 0.44 mM potassium phosphate, 1.3 mM calcium chloride, 1 mM magnesium sulfate, 4.2 mM sodium bicarbonate and 20 mM HEPES (4-[2-hydroxyethyl]-1-piperazineethanesulfonic acid). Note that this particular dye was chosen for our investigation in view of its slow internalization rate—an important characteristic for maintaining high membrane labeling specificity without running the risk of co-labeling subcellular organelles. The staining reaction was allowed to take place for 15 min in a dark environment, after which the enclosure was gently washed with HBSS.

**Microbubble supplementation.** To provide artificial nucleation sites for instigation of sonoporation during ultrasound exposure, lipid-shelled microbubbles were injected into the observation window after cell membrane staining (Fig. 1b, Step 4). Targestat P commercial-grade microbubbles (TS-108, Targeson, San Diego, CA, USA) were used in this work; they had an average diameter of 2.2  $\mu$ m, with less than 1.7% of the microbubble population larger than 5  $\mu$ m. The microbubbles were added at a density of 150,000 bubbles/mL, and thus, the average cell-to-bubble ratio was approximately 1:1. To facilitate microbubble adhesion to the apical surface of the cell,

the cell chamber was flipped upside down for 15 min (Fig. 1b, Step 5), so as to allow buoyant forces to lift the microbubbles toward the anchored fibroblasts. The cell chamber was then gently reverted to its original upright position. Subsequently, the temporary enclosure of the observation window was removed by using forceps to take away the polystyrene coverslip (Fig. 1b, Step 6), and the cell chamber was gently filled with HBSS to a working volume of 25 mL. The cell chamber was placed onto our customized imaging platform within 10 min for experimentation.

**Extracellular calcium ion depletion.** To gain comparative insight into post-sonoporation membrane recovery dynamics, an experiment was conducted in the absence of extracellular calcium ions ( $\text{Ca}^{2+}$ ), which are known to play an active role in membrane recovery processes. For this experiment, the cell loading procedure was the same as for the other experiments, except that a  $\text{Ca}^{2+}$ -free HBSS buffer containing 120 mM NaCl, 3 mM KCl, 3 mM magnesium chloride and 20 mM HEPES was used as the cell chamber buffer after staining. Also, 5 mM ethylene glycol tetraacetic acid (E-3889, Sigma-Aldrich, St. Louis, MO, USA) extracellular  $\text{Ca}^{2+}$  chelators were added to the buffer solution to inactivate  $\text{Ca}^{2+}$  externalized from the cell due to intrinsic ion transport. Note that for this experiment, a 5-min wait period was allowed after the addition of  $\text{Ca}^{2+}$ -free buffer for the chelation reaction to take effect before exposure.

#### Ultrasound exposure procedure

**Pulsing parameters.** For this investigation, a short-duration pulse waveform was used (generated using arbitrary waveform generator). The waveform's center frequency was 1 MHz (*i.e.*, in line with the transducer's center frequency), and the pulse length was set to be 10 cycles. These settings yielded a pulse duration of 10  $\mu\text{s}$ . Pulse triggering was carried out manually during experimentation to facilitate single-pulse ultrasound activation of microbubble pulsation or collapse. The waveform amplitude was adjusted to a level that corresponded to a nominal peak negative pressure of 0.85 MPa, as calibrated by hydrophone measurements described below. This pressure value, well considered to be within the typical levels used in imaging diagnostics (Humphrey 2007), was chosen so as not to trigger cavitational activities in a microbubble-free medium.

**Field calibrations.** To characterize the acoustic exposure conditions *in situ*, free-field mapping of the peak negative pressure in front of the waveguide (with tip detached) was performed inside a 37°C water bath using a needle hydrophone (HNR-0500, ONDA, Sunnyvale, CA, USA) that was facing the nose of the wave-

guide. Note that the needle hydrophone was mounted onto a three-axis scan stage (ASTS-01, ONDA) to facilitate high-precision positioning. Also, to avoid needle tip contact, the hydrophone holder included an *ad hoc* guard rail in the form of a wooden straw whose length was 1 mm longer than the needle hydrophone. In other words, all field measurements were conducted at a minimum distance of 1 mm from the nose of the waveguide.

As illustrated in Figure 2a (xz-plane map), the axial maximum of the free-field peak negative pressure was approximately 4 mm away from the waveguide nose. Because this value was rather close to the physical length of the detachable waveguide tip, the pressure magnitude at the free-field axial maximum can be inferred as the incident level of ultrasound field impinging on the cell chamber. Figure 2b shows the single-pulse waveform detected by the hydrophone at the free-field axial maximum. The peak negative pressure was found to be 0.85 MPa. This value was regarded as the nominal peak negative pressure in our investigation.

To examine the homogeneity of incident ultrasound field along the surface of the cell chamber, 40°-angle cross-sectional mapping of the peak negative pressure was carried out at the free-field axial maximum. As illustrated in Figure 2a (xy-plane map), the  $150 \times 150\text{-}\mu\text{m}^2$  area (marked by the dashed box) corresponding to the largest scan plane size used in this work only had limited variations (1%) in the free-field peak negative pressure. Note that standing waves (with pressure anti-nodes up to twice the free-field value) would inevitably emerge *in situ* because of the strong acoustic reflection at the base of our cell chamber, which was essentially interfaced with the microscope's lens. Nevertheless, we restrained the confounding effect of these standing waves on our experimental results by using a single short ultrasound pulse (10 cycles) to instigate cavitational activity. Indeed, this uncertainty in the *in situ* acoustic pressure would not affect the validity of our findings because all our observations were directly attributed to episodes of microbubble pulsation or collapse.

#### Confocal microscopy procedure

**Imaging parameters.** To elicit the fluorescence of cell membrane (stained by the CellMask Orange dye), a laser excitation wavelength of 543 nm was used; for signal detection, a reception band of 555–643 nm was used. A 40 $\times$  oil lens (420461-9910, Carl Zeiss) was used for image capture. It had a numerical aperture of 1.3 and a refractive index of 1.518. As discussed in the Results section, the confocal microscope's pinhole size, pixel dwell time and image size were varied to adjust the frame rate of planar raster scans as necessary to image membrane perforation (a fast membrane

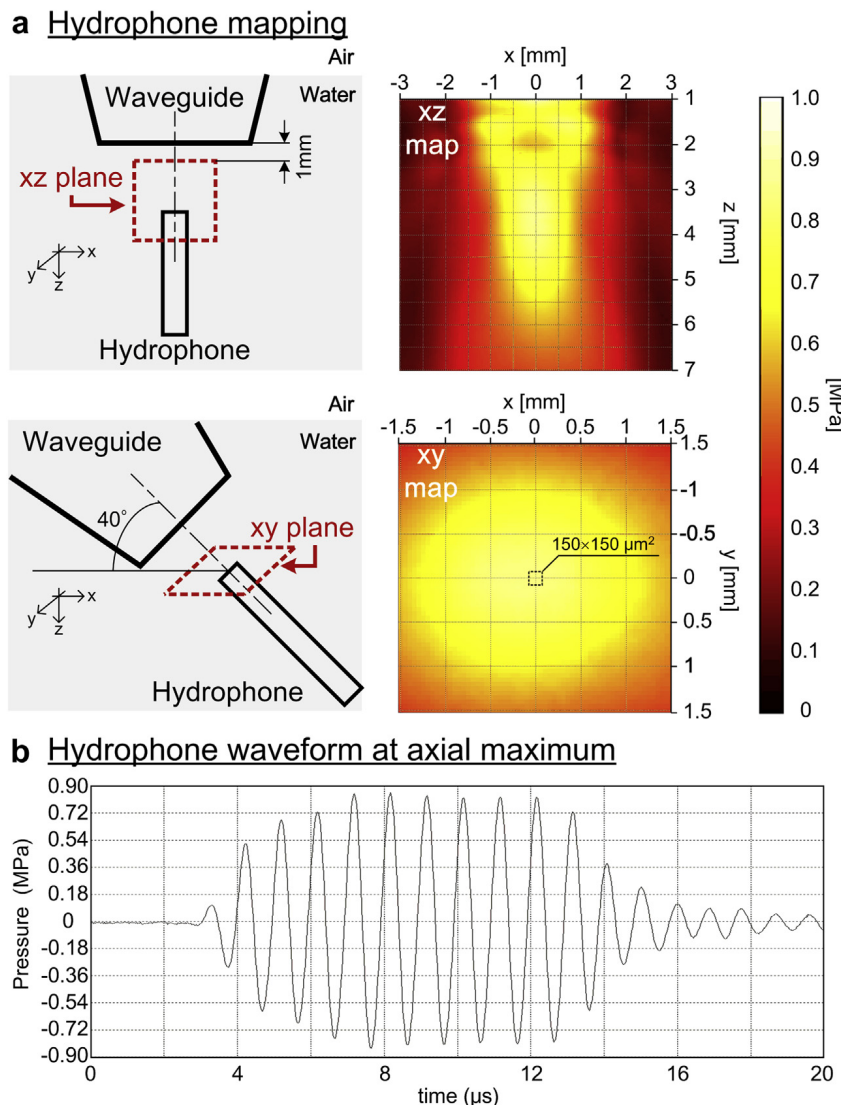
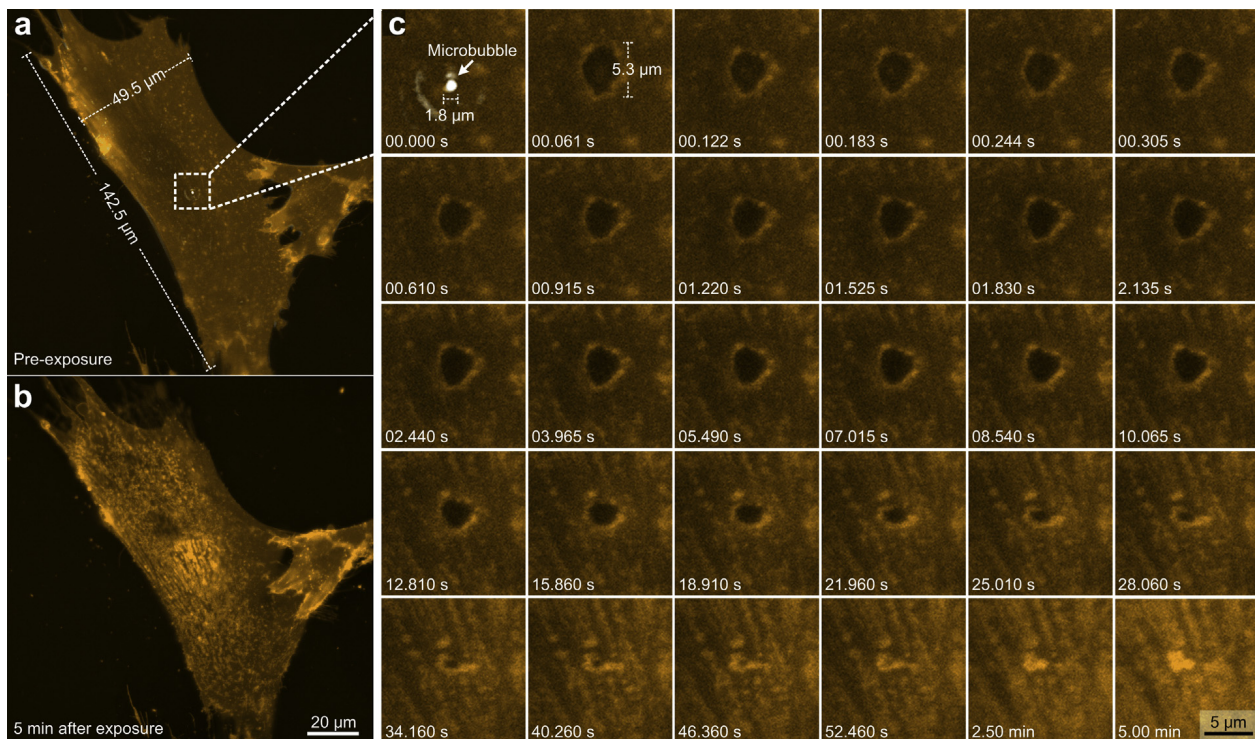


Fig. 2. Free-field pressure maps generated by the ultrasound waveguide, as measured using a needle hydrophone. (a) Peak negative pressure measurements along the  $xz$ - and  $xy$ -planes. Schematics of the measurement configuration are given on the left, and measurement results along the two planes on the right. (b) Pressure waveform detected by the hydrophone at the axial maximum at  $(x, y, z) = (0, 0, 4)$  mm.

process) and post-sonoporation recovery (a relatively slower membrane process).

**Scan configurations.** In this work, the scan plane positions were set to correspond to the apical and basal surfaces of the cell so as to monitor membrane dynamics adjacent to and away from the microbubble (adhered to the apical side). In addition to performing planar scans of the cell, single-line scans were conducted to capture the fast-changing temporal dynamics of the membrane along one line of interest along an image plane. Moreover, bright-field images were acquired in parallel to locate the microbubble position *in situ*. Cine loops were then formed to visualize the time-course dynamics of membrane-level processes in sonoporation.

**Data analysis.** Image frames were imported into ImageJ (Version 1.47n, National Institutes of Health, Bethesda, MD, USA) for quantitative analysis of sonoporation features. Specifically, the pore area and its long-axis diameter were measured for multiple episodes of sonoporation ( $N = 7$ ) by demarcating the pore contour in each frame and measuring the contour size. A time profile of these measures was formed correspondingly, and temporal-peak values were identified. Using the GraphPad Prism software (Version 5, GraphPad Software, La Jolla, CA, USA), pore measurements for cells with successful resealing were statistically compared against those that failed to reseal (based on the Student *t*-test). Also, saturation growth regression was performed to estimate the perforation time constant for each episode of



**Fig. 3.** Time-series confocal fluorescence images revealing localized membrane perforation and recovery induced by ultrasound-triggered collapse of a single microbubble. (a, b) Whole-cell images of a fibroblast (a) before exposure and (b) 5 min after exposure. The scan plane was centered at the apical surface of the cell. The membrane is indicated by orange fluorescence; the microbubble is depicted by the overlaid gray-scale contrast. (c) Series of membrane fluorescence images for a  $15 \times 15\text{-}\mu\text{m}^2$  region ( $128 \times 128$  pixels) centered about the microbubble adhered to the cellular membrane. This image set was acquired at a rate of 16.39 fps (61-ms frame period), using a 599- $\mu\text{m}$  pinhole size and 1.58- $\mu\text{s}$  pixel dwell time.

sonoporation (between the onset of pore formation and the instant when pore area reached a maximum). To quantify recovery dynamics after sonoporation, the post-resealing scar area was gauged as similar to the pore size measurements. As well, the resealing time constant was estimated through an exponential decay regression (from the instant at which pore area reached a maximum to the time point of pore closure). The time constants and observed resealing outcomes (success or failure) were correlated against temporal-peak pore area using Spearman's non-parametric analysis to determine their relationship.

## RESULTS

### *Localized perforation of cell membrane upon microbubble collapse*

Spatially localized membrane perforation was observed immediately upon the application of a 10-cycle ultrasound pulse to instigate the collapse of microbubbles that had passively adhered to the cell membrane. As a representative example, [Supplementary Video 1](#) (acquired at the rate of 16.39 frames/s [fps]) shows a cine loop of membrane perforation induced by a single collapsing microbubble that was originally adhered to the apical surface of an anchored fibroblast before ultrasound

exposure. The exact position of this field of view is depicted in [Figure 3](#), which also provides a time series image set of the perforation site.

Three salient observations can be noted from [Supplementary Video 1](#) and [Figure 3](#): (i) pore creation was synchronized with the time course of microbubble collapse; (ii) the resulting pore size ( $5.3\text{-}\mu\text{m}$  long-axis diameter) was greater than the microbubble size ( $1.8\text{-}\mu\text{m}$  diameter); (iii) membrane resealing commenced within 5 s after the incidence of sonoporation and was completed within 1 min. It should be emphasized that the perforation process was confined to a local region of the cell membrane. Indeed, the size of the perforation site was much smaller than the fibroblast's dimensions (length =  $142.5\text{ }\mu\text{m}$ , width =  $49.5\text{ }\mu\text{m}$ ). In general, as depicted in [Figure 4a](#) (left), the temporal-peak pore area generated using our single-microbubble mediated approach was less than  $30\text{ }\mu\text{m}^2$  for cases with successful resealing ( $N = 7$ ). The corresponding long-axis diameter was smaller than  $6.5\text{ }\mu\text{m}$  ([Fig. 4b](#), left box).

### *Sonoporation: Also inducible by oscillating microbubbles*

Besides ultrasound-triggered microbubble collapse (which signifies inertial cavitation), ultrasound-initiated

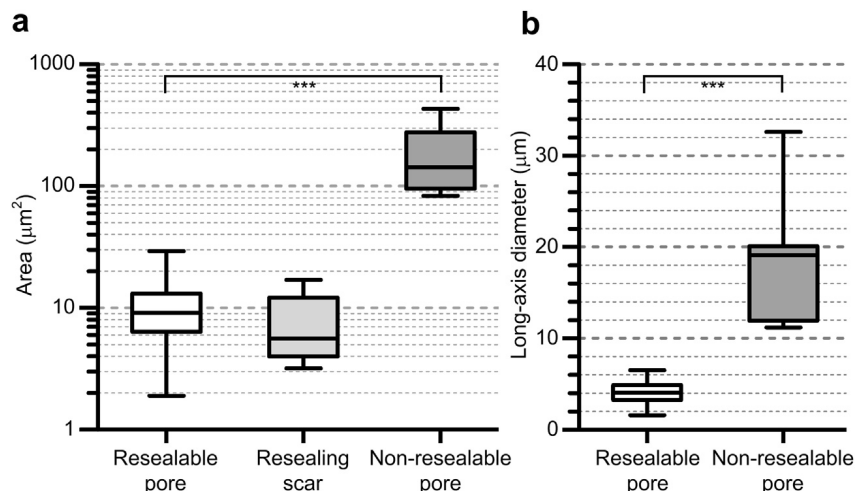


Fig. 4. Pore sizes generated using single microbubble-mediated sonoporation ( $N = 7$ ). (a) Box-whisker plots for (left) temporal peak area for pores with successful resealing, (middle) post-resealing scar area, (right) temporal peak area for pores that failed to reseal. (b) Temporal peak long-axis diameter for pores that were (left) resealable and (right) non-resealable. Error bars denote smallest and largest values in the data set. \*\*\*Statistically significant difference ( $p < 0.001$ ).

microbubble pulsations (corresponding to stable cavitation) were also found to be capable of inducing membrane perforation. Figure 5 illustrates how temporary membrane disruption (on the apical side of the cell) was synchronized with a vibrating microbubble. In this case example, the microbubble was originally

2.2  $\mu\text{m}$  in size before ultrasound exposure. The bright-field image shows that when a single ultrasound pulse was applied (at the 0-s time point), the microbubble did not collapse, but was triggered to pulsate with a minimum diameter that was measured to be 1.2  $\mu\text{m}$ . Also, the microbubble was deflected from its original position

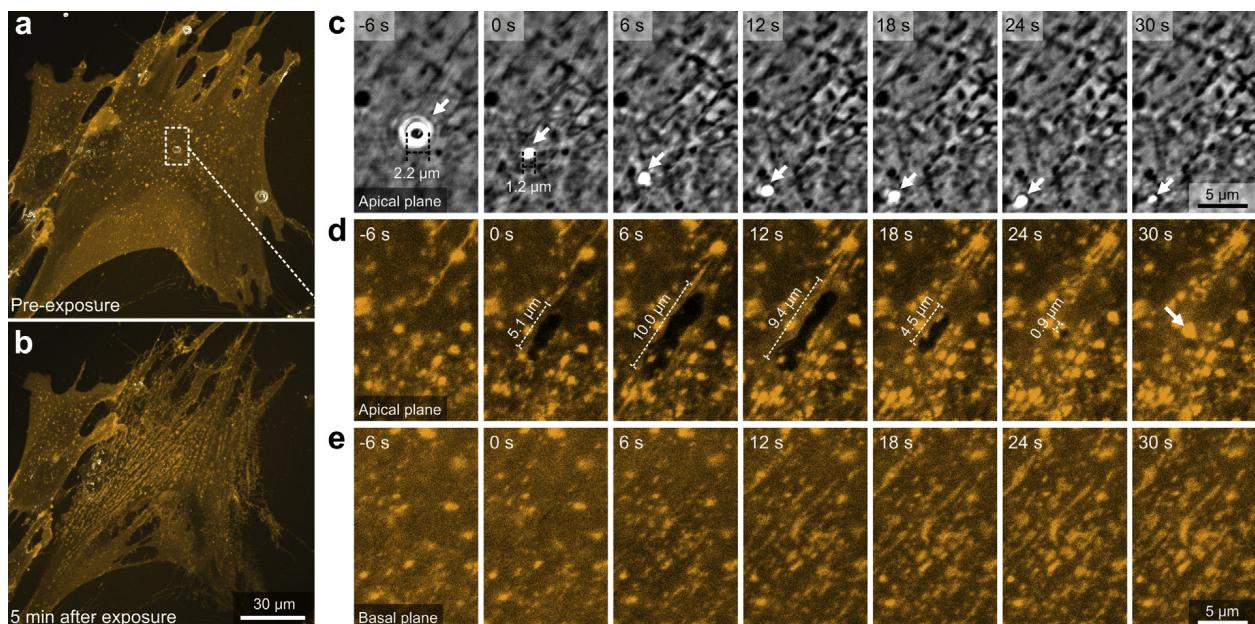


Fig. 5. Ultrasound-triggered microbubble pulsation can induce membrane tearing, as indicated by time-lapse membrane fluorescence imaging (6-s frame period, 97- $\mu\text{m}$  pinhole size, 2.55- $\mu\text{s}$  pixel dwell time). (a, b) Whole-cell images of the apical surface of the fibroblast before and 5 min after exposure. (c) Bright-field image series showing an episode of microbubble pulsation and displacement over a 30-s period (triggered by a single ultrasound pulse applied at 0 s). Original microbubble diameter was 2.2  $\mu\text{m}$ , and its minimum diameter was 1.2  $\mu\text{m}$  over the course of pulsation. (d) Confocal image series showing transient membrane tearing on the apical surface of the cell as the vibrating microbubble was displaced from the original position. (e) The basal surface remained intact.

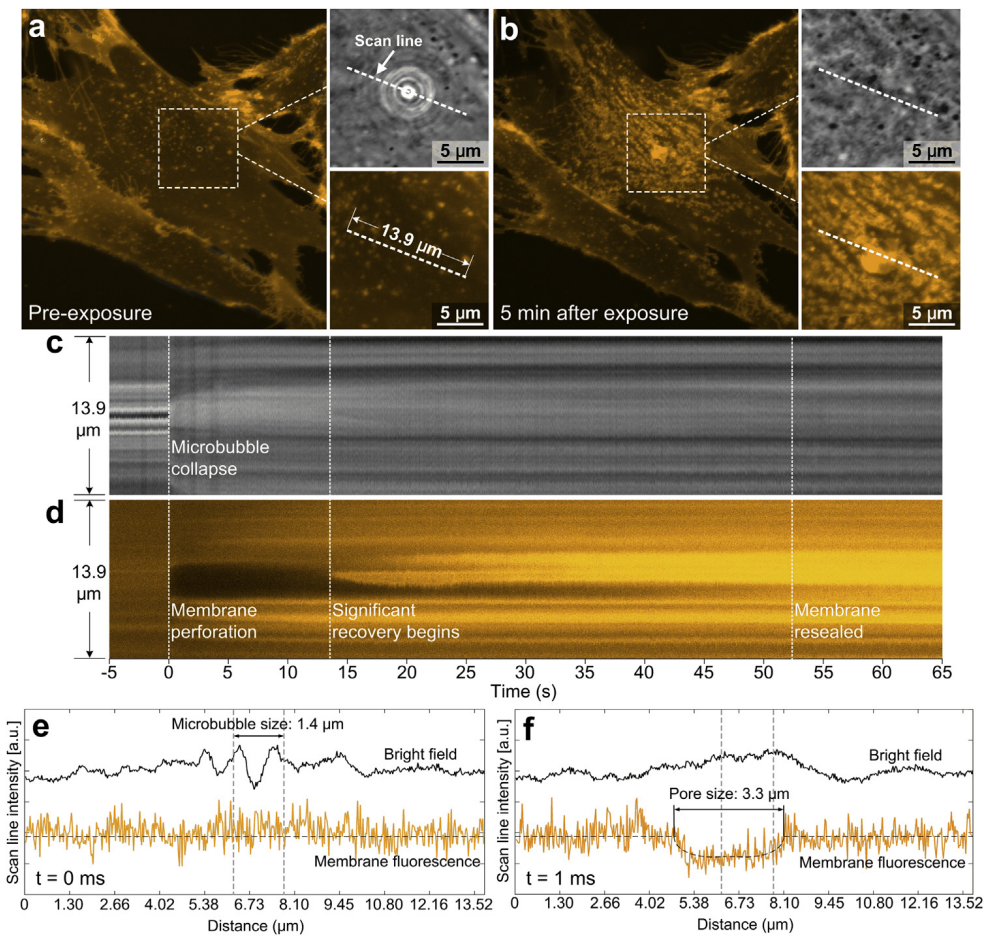


Fig. 6. (a, b) Single-line confocal scans on the apical surface of the cell illustrating the time-course dynamics of membrane perforation and recovery in sonoporation. Scan line position ( $13.9\text{ }\mu\text{m}$  in length, centered about the microbubble) is depicted in the apical plane confocal and bright-field images (a) before exposure and (b) 5 min after exposure. (c, d) Time sweep plots of bright-field contrast (c) and membrane fluorescence (d) for the specified scan line (1-ms temporal resolution;  $304\text{-}\mu\text{m}$  pinhole size;  $0.79\text{-}\mu\text{s}$  pixel dwell time). (e, f) Scan line intensity plots of bright-field contrast and membrane fluorescence at (e) the time of ultrasound application (0 ms) and (f) the next sampling time point (1 ms). In this example, the collapse of a  $1.4\text{-}\mu\text{m}$ -diameter microbubble (at 0 ms) resulted in the creation of a  $3.3\text{-}\mu\text{m}$ -diameter pore (at 1 ms).

and drifted toward the lower-left direction in the field-of-view. Over this process, membrane tearing along the apical surface was apparent, while the basal side of the cell remained intact. The maximum long-axis length of this tearing was found to be  $10.0\text{ }\mu\text{m}$  (observed 6 s after ultrasound pulsing). Resealing took place afterward and was completed after 30 s.

#### Membrane perforation is a rapid process

As can be observed from [Supplementary Video 1](#), the onset of membrane perforation was a rapid process. To further exemplify this observation, we conducted a single-line scan of the membrane dynamics at a temporal resolution of 1 ms. As shown in [Figure 6](#), the scan line was placed across the microbubble to capture the correspondence between the onset of microbubble collapse and membrane perforation. In this case, before

exposure to ultrasound, the microbubble had a diameter of  $1.4\text{ }\mu\text{m}$ . At the time of ultrasound pulsing, the microbubble collapsed immediately, and the membrane was perforated concurrently. Note that 1 ms after ultrasound pulsing, pore size was measured to be  $3.3\text{ }\mu\text{m}$ , which was 2.4 times greater than the microbubble size. As such, it can be inferred that a blasting effect was generated on the cell membrane by the ultrasound-induced microbubble collapse.

Additional insight into the rapid nature of membrane perforation can be gained from [Figure 7a](#), in which time traces of the measured pore area are plotted for seven sonoporation episodes induced using our single microbubble-mediated approach. As can be observed, the first 5 s after the onset of perforation was generally the time window in which the pore would expand rapidly toward its maximum size. Indeed, except for one case (the

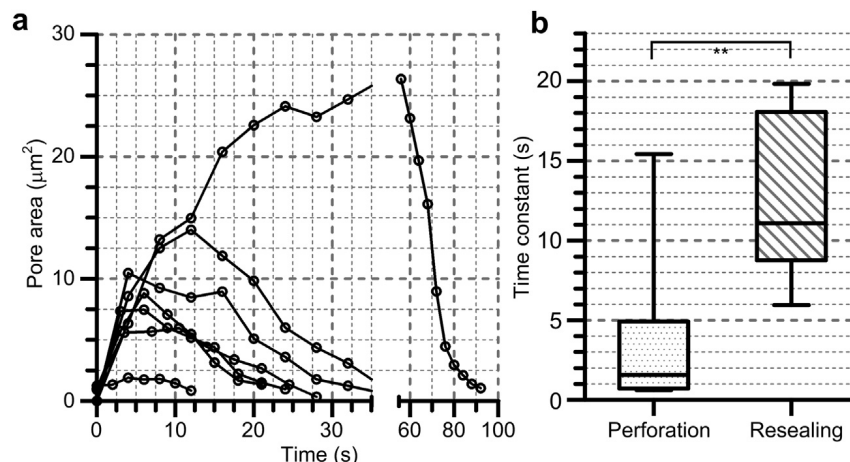


Fig. 7. (a) Temporal profile of pore area for seven different sonoporated cells that resealed over time. (b) Time constants for perforation and pore resealing, as determined respectively from saturation growth regression and exponential decay regression of the temporal curves shown. \*\*Statistically significant difference ( $p < 0.01$ ).

uppermost curve in Fig. 7a), the pore stopped expanding within 12 s after sonoporation. The perforation time constant, as determined from saturation growth regression analysis, was found to be generally below 5 s, except for the outlier case mentioned (see box-whisker plot given in Fig. 7b, left box). Note that no statistically significant correlation ( $\rho = 0.4286$ ) was found between the perforation time constant and temporal-peak pore area.

#### Membrane recovery: Tens of seconds in duration and a multi-faceted process

Resealing of the perforation site generally commenced within 10 s after the onset of perforation. As shown in the time traces of Figure 7a, the time from the instant at which pore size reached a maximum to the completion of pore closure was generally on the order of tens of seconds. For the seven sonoporation episodes, their resealing time constant derived from an exponential decay regression analysis was found to range between 6 and 20 s (see Fig. 7b, right box). This time constant was statistically correlated ( $\rho = 0.8571$ ,  $p < 0.05$ ) with temporal-peak pore area for a particular episode of sonoporation. Such a correlation is after all expected because it is reasonable for larger pores to require a longer time to reseal.

The course of action involved in post-sonoporation resealing was found to be rather multi-faceted from a biological standpoint. As can be noted from Supplementary Video 1 as well as Figures 3 and 5, during the recovery stage, the rim of the disrupted membrane exhibited a stronger fluorescence level, which indicates a local increase in phospholipid content. Also, after membrane resealing was completed, the original perforation site exhibited strong fluorescence, and this area was measured to be on the same order as the temporal-peak pore area (see Fig. 4a, middle box). These observations suggest

that post-sonoporation scarring of the membrane may emerge. Another observation of interest is that, although membrane perforation induced by ultrasound-triggered microbubble collapse or pulsation was localized, other segments of the cell membrane may be disrupted over the process. In particular, away from the perforation site, the membrane exhibited a striated pattern post-exposure that was not observed pre-exposure. Indeed, as shown in Figures 3b and 5b, such a membrane striation pattern was evident over the surface of the entire sonoporated cell.

#### Membrane may not reseal if pore size is too large

It is worth emphasizing that post-sonoporation membrane resealing might fail for excessively punctured perforation sites. Evidence of this phenomenon is given in Supplementary Video 2, which features a cine loop of how a sonoporated cell has not resealed its perforation site after 6 min into the sonoporation episode (frame period: 3 s). Indeed, a time-lapse enlargement of the pore was apparent starting 10 s after the onset of sonoporation, and this process lasted until 3.5 min into the episode, after which the pore slowly began to undergo resealing. A still-frame rendering of this observation is provided in Figure 8. Note that the apical pore was measured to be  $32.6 \mu\text{m}$  in long-axis diameter (generated by ultrasound-triggered collapse of a  $1.5\text{-}\mu\text{m}$ -diameter microbubble). Another point worth noting in this example is that in addition to excessive puncturing on the apical surface of the cell, mild but reversible membrane tearing on the basal side of the cell can also be observed. The maximum size of the basal tear was  $12.5 \mu\text{m}$ , a value that is in line with our microbubble pulsation-induced membrane tear shown in Figure 5. Such a difference between apical and basal pore sizes

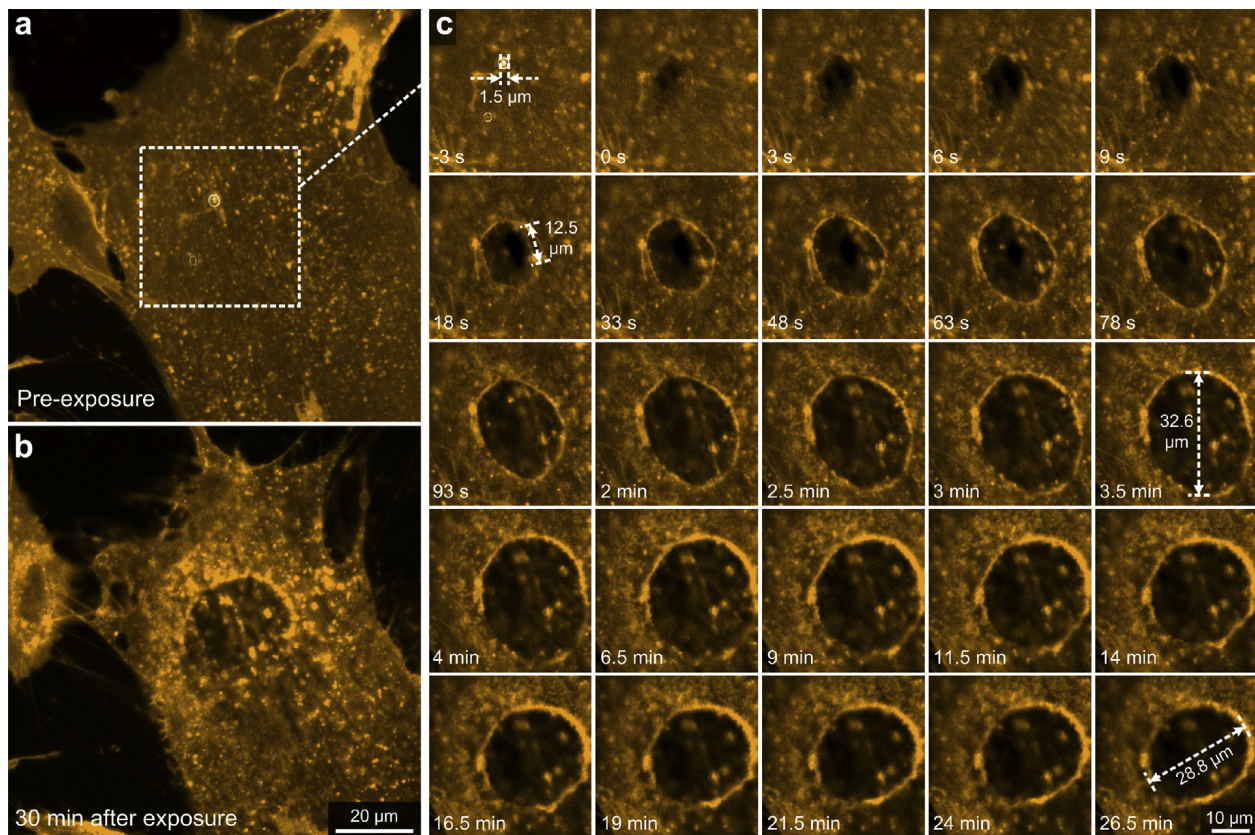


**Fig. 8.** Membrane perforation induced by ultrasound-triggered microbubble collapse can be unrecoverable for large pore sizes. (a, b) Whole-cell confocal fluorescence images (a) before exposure and (b) 30 min after exposure for an illustrative case of unsuccessful post-sonoporation membrane resealing. (c) Corresponding image series before and after microbubble collapse for the field of view marked in (a). These images were acquired in a 3-s frame period using 199-μm pinhole size and 0.50-μs pixel dwell time.

may help explain why the apical pore has not resealed, even 30 min after exposure.

To characterize the relationship between resealing outcome and pore size, seven different episodes of sonoporation with failed resealing were identified, and their temporal-peak pore area and long-axis diameter were measured. Compared to cases with successful resealing, sonoporated cells that failed to reseal exhibited a substantially larger pore area that was one order of magnitude higher (see Fig. 4a, right box). Also, the long-axis pore diameters in these cases were all larger than 10 μm (see Fig. 4b, right box). These results indicate a strong correlation between pore size and failure of post-sonoporation resealing, and this was statistically confirmed through a Spearman's rank correlation analysis that examined the size distribution of both resealable pores and non-resealed ones ( $\rho = 0.8603$ ,  $p < 0.001$ ).

#### *Extracellular Ca<sup>2+</sup> chelation inhibited resealing of sonoporation site*

Regardless of whether post-sonoporation membrane resealing was ultimately successful, the presence of

extracellular Ca<sup>2+</sup> was found to be critical to initiation of the recovery process. When extracellular Ca<sup>2+</sup> was depleted, cellular recovery features were not apparent. **Supplementary Video 3** and **Figure 9** respectively show a cine loop and a time-series compilation of membrane topography images for an anchored fibroblast that was sonoporated in the absence of extracellular Ca<sup>2+</sup>. It can be observed that after the onset of membrane perforation, the pore had not resealed after 20 min (in contrast to typical completion of resealing within 1 min). Also, no indication of membrane recovery initiation can be found (e.g., no thickening was observed at the rim of the disrupted membrane). Indeed, pore size gradually expanded over time: its long-axis length was 5.6 μm initially, but increased to 8.7 μm after 20 min.

## DISCUSSION

#### *Primary contribution: Direct visualization of membrane dynamics in sonoporation*

Characterizing membrane behavior in sonoporation is of scientific interest because the plasma membrane is

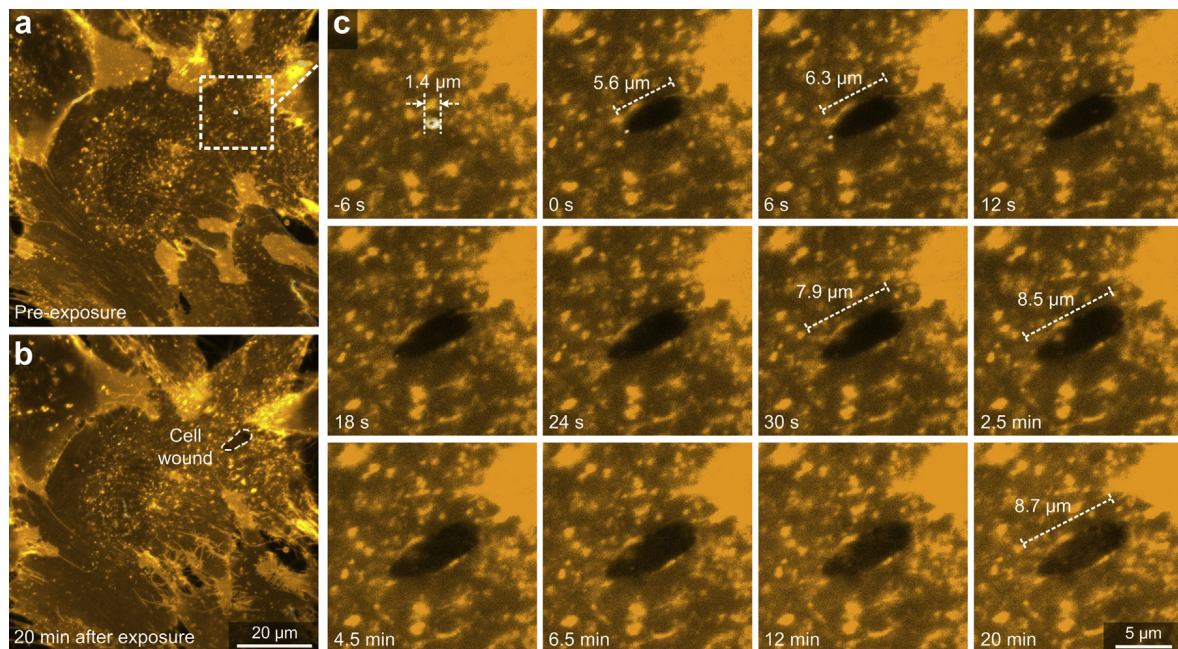


**Fig. 9.** Membrane fluorescence image series for an anchored fibroblast that was sonoporated in the absence of extracellular  $\text{Ca}^{2+}$ . (a, b) Apical plane whole-cell images (a) before exposure and (b) 20 min after exposure. (c) Time series of images for the period between 6 s before exposure and 20 min after exposure. Note that the perforation site revealed no signs of recovery. The frame period was 6 s using a 97- $\mu\text{m}$  pinhole size and 2.55- $\mu\text{s}$  pixel dwell time.

well regarded as a fluidic structure and is not a passive, rigid barrier. In line with this objective, our real-time cine loops have provided a direct visualization of how the onset of plasma membrane perforation is synchronized with a cavitating microbubble ([Supplementary Video 1](#)).

These direct observations reveal that sonoporation can be realized by a microbubble undergoing physical collapse (inertial cavitation; see [Fig. 3](#)) or non-collapsing pulsation (stable cavitation; see [Fig. 5](#)). They also illustrate how membrane resealing, if successful, would typically be completed within 1 min after the onset of sonoporation ([Fig. 6](#)). This latter finding is especially relevant to underscoring the prevailing perception that sonoporation is a transitory phenomenon ([Liang \*et al.\* 2010](#)). Further analysis of our imaging observations allowed us to gain quantitative insight into the dynamics of perforation and resealing in sonoporation. Temporal-peak pore area was found to be a key factor influencing resealing outcome ([Fig. 4](#)) and recovery duration ([Fig. 7](#)).

To our knowledge, this investigation represents the first demonstration of the temporal course of membrane-level events involved in sonoporation. It can in essence be considered an effort to acquire new epitomizing evidence on the spatiotemporal dynamics of sonoporation. It is uniquely positioned between previous observations that have revealed phenomena either upstream or downstream of the actual perforation process. For instance, our results are distinguished from

upstream findings that illustrate how cavitation-induced jetting would lead to membrane puncturing ([Ohl \*et al.\* 2006](#)), as well as how the extent of membrane effect can be modulated by controlling the microbubble's distance from the membrane ([Zhou \*et al.\* 2012](#)). They also differ from downstream observations that have identified episodes of sonoporation based on whether internalization of fluorescent markers took place ([Kooiman \*et al.\* 2011](#); [van Ruijssevelt \*et al.\* 2013](#)).

#### New insights on post-sonoporation membrane recovery processes

In addition to serving as unequivocal evidence of sonoporation, our experimental findings have provided new insight into physiological factors that influence post-sonoporation membrane recovery. In particular, we found that membrane resealing is not necessarily a definite process that is always executed successfully. In cases where pore size was excessive, the sonoporated membrane was observed to remain perforated 30 min into the onset of sonoporation ([Supplementary Video 2](#) and [Fig. 8](#)). Also, for post-sonoporation resealing to be initiated, the presence of extracellular  $\text{Ca}^{2+}$  is vital ([Supplementary Video 3](#) and [Fig. 9](#)). On the basis of these findings, it can be readily deduced that membrane resealing is inherently a complex process that depends on various biophysical factors.

Our direct observations have also provided new clues to the course of action involved in post-sonoporation

membrane resealing. One common topographic feature of sonoporated cells undergoing membrane resealing is the emergence of a thickened rim at the perforation site (Figs. 3, 5 and 8). The temporal progression of this rim was found to correspond to the pore closure action. Regardless of whether membrane integrity is ultimately restored, pore rim thickening is likely to be an essential feature of membrane resealing because such a feature is not present when the resealing process is inhibited *via* extracellular Ca<sup>2+</sup> depletion (Fig. 8). On review of the cell biology literature, we found that this feature is essentially similar in appearance to the concentric zones of actin and myosin observed in recovering single-cell wounds (Benink and Bement 2005). As actin and myosin are essentially components of a cell's cytoskeleton, it may well be possible that post-sonoporation membrane resealing is a cytoskeleton-dependent process.

Two other recovery-related membrane features of our results are worth noting: (i) scarring of successfully resealed perforation sites, and (ii) striation of the membrane surface away from the perforation site (Figs. 3 and 5). The first feature may be attributed to the closure action of the thickened rim, or it may be the result of other mechanisms such as exocytotic patching of intracellular vesicles and organelles that are also rich in phospholipids (Sonnenmann and Bement 2011). Explanation of the second feature would require a more detailed analysis of the cell's cytomechanical balance after sonoporation. It may well be possible that the cytoskeleton, which plays a central role in maintaining the structural integrity of the cell, is directly involved in eliciting the membrane striation patterns.

## CONCLUSIONS

When exploiting sonoporation for biomedical applications, membrane perforation and its subsequent recovery are often regarded as routine processes that are presumed to take place because trans-membranous transport is known to be enhanced on an immediate basis. Although such an assumption is not invalid, it inherently omits membrane-level dynamics, which are important from a biophysical perspective. To gain insight into this topic, we devised a customized ultrasound exposure platform with real-time confocal microscopy capabilities to acquire new direct evidence of how, at the single-cell level, membrane perforation typically occurs in an episode of single microbubble collapse triggered by a single ultrasound pulse. In addition, we directly observed how post-sonoporation membrane recovery takes place *in situ*. Taken together, these experimental findings serve well to highlight the transitory nature of sonoporation at the membrane level. We anticipate that our series of direct observations presented here can serve as

mechanistic motivation for further efforts that seek to optimize the realization of sonoporation from a more biologically centered perspective in which the biophysical pathways involved in membrane perforation are taken into account.

**Acknowledgments**—This work has been supported in part by the Hong Kong Innovation and Technology Fund (ITS/292/11) and the University of Hong Kong (201111159091). We are grateful to Dr. Wai-Hung Sit and Ms. Helen Leung for their helpful technical advice on experimental design.

## SUPPLEMENTARY DATA

Supplementary data related to this article can be found online at <http://dx.doi.org/10.1016/j.ultrasmedbio.2013.08.003>.

## REFERENCES

- Benink HA, Bement WM. Concentric zones of active RhoA and Cdc42 around single cell wounds. *J Cell Biol* 2005;168:429–439.
- Deng CX, Sieling F, Pan H, Cui J. Ultrasound-induced cell membrane porosity. *Ultrasound Med Biol* 2004;30:519–526.
- Duvshani-Eshet M, Baruch L, Kesselman E, Shimoni E, Machluf M. Therapeutic ultrasound-mediated DNA to cell and nucleus: Bio-effects revealed by confocal and atomic force microscopy. *Gene Ther* 2006;13:163–172.
- Fan Z, Kumon RE, Park J, Deng CX. Intracellular delivery and calcium transients generated in sonoporation facilitated by microbubbles. *J Control Release* 2010;142:31–39.
- Fan Z, Liu H, Mayer M, Deng CX. Spatiotemporally controlled single cell sonoporation. *Proc. Natl Acad Sci USA* 2012;109: 16486–16491.
- Ferrara K, Pollard R, Borden M. Ultrasound microbubble contrast agents: Fundamentals and application to gene and drug delivery. *Annu Rev Biomed Eng* 2007;9:415–447.
- Geers B, Dewitte H, de Smedt SC, Lentacker I. Crucial factors and emerging concepts in ultrasound-triggered drug delivery. *J Control Release* 2012;164:248–255.
- Hernot S, Klibanov AL. Microbubbles in ultrasound-triggered drug and gene delivery. *Adv Drug Deliv Rev* 2008;60:1153–1166.
- Humphrey VF. Ultrasound and matter: Physical interactions. *Prog Biophys Mol Biol* 2007;93:195–211.
- Juffermans LJM, van Dijk A, Jongenelen CAM, Drukarch B, Reijerkerk A, de Vries HE, Kamp O, Musters RJP. Ultrasound and microbubble-induced intra- and intercellular bioeffects in primary endothelial cells. *Ultrasound Med Biol* 2009;35:1917–1927.
- Kooiman K, Foppen-Harteveld M, van der Steen AFW, de Jong N. Sonoporation of endothelial cells by vibrating targeted microbubbles. *J Control Release* 2011;154:35–41.
- Kudo N, Okada K, Yamamoto K. Sonoporation by single-shot pulsed ultrasound with microbubbles adjacent to cells. *Biophys J* 2009; 96:4866–4876.
- Kumon RE, Aehle M, Sabens D, Parikh P, Han YW, Kourennyi D, Deng CX. Spatiotemporal effects of sonoporation measured by real-time calcium imaging. *Ultrasound Med Biol* 2009;35:494–506.
- Liang HD, Tang J, Halliwell M. Sonoporation, drug delivery, and gene therapy. *Proc Inst Mech Eng H* 2010;224:343–361.
- Liu Y, Miyoshi H, Nakamura M. Encapsulated ultrasound microbubbles: Therapeutic application in drug/gene delivery. *J Control Release* 2006;114:89–99.
- Mehler-Humbert S, Bettinger T, Yan F, Guy RH. Plasma membrane poration induced by ultrasound exposure: Implication for drug delivery. *J Control Release* 2005;104:213–222.
- Meijering BDM, Juffermans LJM, van Wamel A, Henning RH, Zuborn IS, Emmer M, Versteilen AMG, Paulus WJ, van Gilst WH, Kooiman K, de Jong N, Musters RJP, Deelman LE, Kamp O. Ultrasound and microbubble-targeted delivery of

- macromolecules is regulated by induction of endocytosis and pore formation. *Circ Res* 2009;104:679–687.
- Nejad SM, Hosseini SMR, Akiyama H, Tachibana K. Optical observation of cell sonoporation with low intensity ultrasound. *Biochem Biophys Res Commun* 2011;413:218–223.
- Nomikou N, McHale AP. Exploiting ultrasound-mediated effects in delivering targeted, site-specific cancer therapy. *Cancer Lett* 2010;296:133–143.
- Ohl CD, Arora M, Iking R, de Jong N, Versluis M, Delius M, Lohse D. Sonoporation from jetting cavitation bubbles. *Biophys J* 2006;91:4285–4295.
- Pan H, Zhou Y, Izadnegahdar O, Cui J, Deng CX. Study of sonoporation dynamics affected by ultrasound duty cycle. *Ultrasound Med Biol* 2005;31:849–856.
- Park J, Fan F, Kumon RE, El-Sayed MEH, Deng CX. Modulation of intracellular  $\text{Ca}^{2+}$  concentration in brain microvascular endothelial cells in vitro by acoustic cavitation. *Ultrasound Med Biol* 2010;36:1176–1187.
- Prentice P, Cuschieri A, Dholakia K, Prausnitz M, Campbell P. Membrane disruption by optically controlled microbubble cavitation. *Nat Phys* 2005;1:107–110.
- Pua EC, Zhong P. Ultrasound-mediated drug delivery. *IEEE Eng Med Biol Mag* 2009;28:64–75.
- Qiu Y, Luo Y, Zhang Y, Cui W, Zhang D, Wu J, Zhang J, Tu J. The correlation between acoustic cavitation and sonoporation involved in ultrasound-mediated DNA transfection with polyethylenimine (PEI) in vitro. *J Control Release* 2010;145:40–48.
- Ross JP, Cai X, Chiu JF, Yang J, Wu J. Optical and atomic force microscopic studies on sonoporation. *J Acoust Soc Am* 2002;111:1161–1164.
- Sankin GN, Yuan F, Zhong P. Pulsating tandem microbubble for localized and directional single-cell membrane poration. *Phys Rev Lett* 2010;105:078101.
- Schlicher RK, Hutcheson JD, Radhakrishna H, Apkarian RP, Prausnitz MR. Changes in cell morphology due to plasma membrane wounding by acoustic cavitation. *Ultrasound Med Biol* 2010;36:677–692.
- Schlicher RK, Radhakrishna H, Tolentino TP, Apkarian RP, Zarnitsyn V, Prausnitz MR. Mechanism of intracellular delivery by acoustic cavitation. *Ultrasound Med Biol* 2006;32:915–924.
- Sonnemann KJ, Bement WM. Wound repair: Toward understanding and integration of single-cell and multicellular wound responses. *Annu Rev Cell Dev Biol* 2011;27:237–263.
- Suzuki R, Oda Y, Utoguchi N, Maruyama K. Progress in the development of ultrasound-mediated gene delivery systems utilizing nanobubbles and microbubbles. *J Control Release* 2011;149:36–41.
- Tran TA, Le Guennec JY, Bougnoux P, Tranquart F, Bouakaz A. Characterization of cell membrane response to ultrasound activated microbubbles. *IEEE Trans Ultrason Ferroelectr Freq Control* 2008;55:44–49.
- Van Ruijsevelt L, Smirnov P, Yudina A, Bouchaud V, Voisin P, Moonen C. Observations on the viability of C6-glioma cells after sonoporation with low-intensity ultrasound and microbubbles. *IEEE Trans Ultrason Ferroelectr Freq Control* 2013;60:34–46.
- Yang F, Gu N, Chen D, Xi X, Zhang D, Li Y, Wu J. Experimental study on cell self-sealing during sonoporation. *J Control Release* 2008;131:205–210.
- Zhao YZ, Luo YK, Lu CT, Xu JF, Tang J, Zhang M, Zhang Y, Liang HD. Phospholipids-based microbubbles sonoporation pore size and reseal of cell membrane cultured in vitro. *J Drug Target* 2008;16:18–25.
- Zhou Y, Shi J, Cui J, Deng CX. Effects of extracellular calcium on cell membrane resealing in sonoporation. *J Control Release* 2008;126:34–43.
- Zhou Y, Yang K, Cui J, Ye JY, Deng CX. Controlled permeation of cell membrane by single bubble acoustic cavitation. *J. Control Release* 2012;157:103–111.